



## Positive current collector for Li||Sb-Pb liquid metal battery



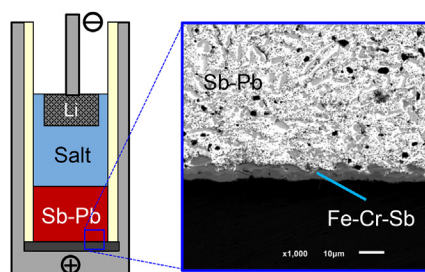
Takanari Ouchi, Donald R. Sadoway\*

Department of Materials Science and Engineering, Massachusetts Institute of Technology, Cambridge, MA, 02139-4307, USA

### HIGHLIGHTS

- A stable current collector for liquid metal battery was discovered.
- No adverse effect of the dissolution of iron or chromium was confirmed.
- The dissolution of nickel causes the capacity decay.
- In situ formation of protective layer on the iron-chromium steel was confirmed.

### GRAPHICAL ABSTRACT



### ARTICLE INFO

#### Article history:

Received 23 January 2017

Received in revised form

18 April 2017

Accepted 29 April 2017

Available online 8 May 2017

#### Keywords:

Liquid metal battery

Corrosion

Sb-Pb alloy

Liquid metal

Stainless steel

### ABSTRACT

Corrosion in grid-scale energy storage devices adversely affects service lifetime and thus has a significant economic impact on their deployment. In this work, we investigate the corrosion of steel and stainless steels (SSs) as positive current collectors in the Li||Sb-Pb liquid metal battery. The erosion and formation of new phases on low-carbon steel, SS301, and SS430 were evaluated both in static conditions and under cell operating conditions. The cell performance is not adversely affected by the dissolution of iron or chromium but rather nickel. Furthermore, the in situ formation of a Fe-Cr-Sb layer helps mitigate the recession of SS430.

© 2017 Published by Elsevier B.V.

## 1. Introduction

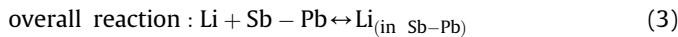
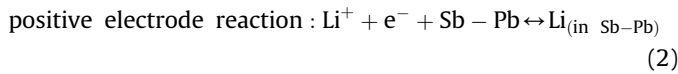
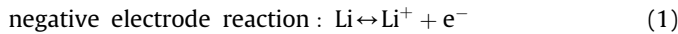
Deployment of grid-scale batteries can result in a more reliable and resilient grid. They also enable the integration of intermittent renewable power sources into baseload generation on the conventional grid and facilitate a variety of functions ranging from peak shifting to frequency regulation. As a candidate for such a storage device, we have developed the liquid metal battery [1]. This consists of a low-density liquid metal negative electrode, an

intermediate-density molten salt electrolyte, and a high-density liquid metal positive electrode, which self-segregate by density into three distinct layers due to their mutual immiscibility. In our previous work, a cell comprising liquid lithium (Li) as the negative electrode, molten lithium halide salt as the electrolyte, and liquid antimony-lead (Sb-Pb) alloy as the positive electrode (Li||Sb-Pb) was demonstrated to be a practical embodiment of the concept [2].

During discharge of the Li||Sb-Pb cell, a liquid Li negative electrode is oxidized to form  $\text{Li}^+$  which transits the electrolyte to the liquid Sb-Pb positive electrode where the  $\text{Li}^+$  electrochemically reduces to neutral metallic Li which alloys with the Sb-Pb. This process is reversed on charging. The overall reaction and half-cell reactions are the following:

\* Corresponding author.

E-mail address: [dsadoway@mit.edu](mailto:dsadoway@mit.edu) (D.R. Sadoway).



The Li||Sb-Pb cell performs with high round-trip coulombic and energy efficiencies (>98%, and >70%, respectively) and wide capability of current density (>1 A cm<sup>-2</sup>).

In the assessment of the utility of such a battery, the most important performance metric is the leveled cost of the system, expressed in equation (4).

$$C_E = \frac{M}{Q_d \cdot E_d \cdot N} + C_e \frac{E_{in}}{E_{out}} \quad (4)$$

where  $C_E$  is leveled cost (\$·kWh<sup>-1</sup>·cycle<sup>-1</sup>),  $M$  capital cost (\$),  $Q_d$  discharge capacity (Ah),  $E_d$  discharge voltage (V),  $N$  life span (cycles),  $C_e$  cost of electricity (\$·kWh<sup>-1</sup>·cycle<sup>-1</sup>),  $E_{in}$  charge energy (kWh), and  $E_{out}$  discharge energy (kWh). As shown in equation (4), the leveled cost varies inversely with service lifetime. In LMBs, there is no physical separator and no irreversible solid degradation mechanism; hence, there is little chance of performance loss through breakdown of active materials. Instead, the life span of LMBs depends mainly on the corrosion resistance of cell components. As part of a comprehensive effort to develop a low-cost, grid-scale electrochemical energy storage device, we investigated corrosion phenomena in the Li||Sb-Pb cell.

Within the electrochemical window of the Li||Sb-Pb cell (0–1.2 V vs. Li), the lithium halide salts are not corrosive to ferrous metals, ceramics, or graphite [3]. Furthermore, a survey of the literature suggested that some ferrous alloys, including low carbon steels and stainless steels (SSs), have sufficient corrosion resistance against Li [4,5]. The Li||Sb-Pb cell fitted with a graphite positive current collector (PCC) exhibited no corrosion from the Sb-Pb positive electrode and little loss of capacity (0.002% per cycle). However, the graphite crucible lacks ductility, which potentially limits scalability and high-volume manufacturing. In this study, we investigated their performance of commonly available steels or

stainless steels in the Li||Sb-Pb cell owing to their low cost, machinability, and ductility.

One of the typical methods to mitigate corrosion of stainless steels in liquid heavy metals, e.g., Pb-Bi, is controlling the oxygen concentration in the liquid alloy [6–8]. The dissolved oxygen with optimal concentration forms on the surface of the solid metal an oxide film, which becomes a protective layer against corrosion. However, due to presence of a liquid Li negative electrode the corrosion process of the PCC is quite complicated in a Li||Sb-Pb cell. The Li metal negative electrode, which has an oxygen affinity that is higher than that of most other elements, dramatically reduces the partial pressure of oxygen in the system. Furthermore, the concentration of Li in the liquid positive electrode varies with state of charge as the battery operates. Therefore, we were motivated to find a new concept for mitigating the corrosion by liquid metals to allow the use of steel and stainless steels as PCCs. In the present work as shown in Fig. 1, we viewed this complicated process from two extreme conditions: (1) fully charged (tantamount to corrosion by lithium-free Sb-Pb alloy), and (2) operating (consideration of the effects of lithium alloying and dealloying). We investigated the corrosion behavior of low carbon steel (1018), Fe-Ni-Cr based stainless steel (SS301), and Fe-Cr based stainless steel (SS430) and analyzed their performance in terms of their material chemistry.

## 2. Materials and methods

The test coupons in this work were iron film (1 mm thick, 99.995%, Alfa Aesar), nickel film (1 mm thick, 99.9945%, Alfa Aesar), chromium cube (6.35 mm, 99.95%, Alfa Aesar), low-carbon steel film (1 mm thick, McMaster-Carr), SS301 film (1 mm thick, McMaster-Carr), and SS430 film (1 mm thick, McMaster-Carr). The compositions of low carbon steel, SS301, and SS430 are listed in Table 1. Test coupons were polished with diamond pastes, 1 μm in diameter. These cells were charged with 0.32 g of Li (99.9%, Sigma Aldrich), 2.1 g of Sb (99.999%, Alfa Aesar), and 8.3 g of Pb (99.999%, Alfa Aesar). The Sb-Pb alloy was prepared with the composition of 30–70 mol%. To evaluate the corrosion behavior in a fully-charged cell, the test coupons were placed in liquid Sb-Pb alloy as shown in Fig. 1 (a). Then, the corrosion behavior of the test coupons in the cell at various charge-discharge conditions was evaluated by passing current through the cells shown in Fig. 1 (b) and (c). A low-carbon

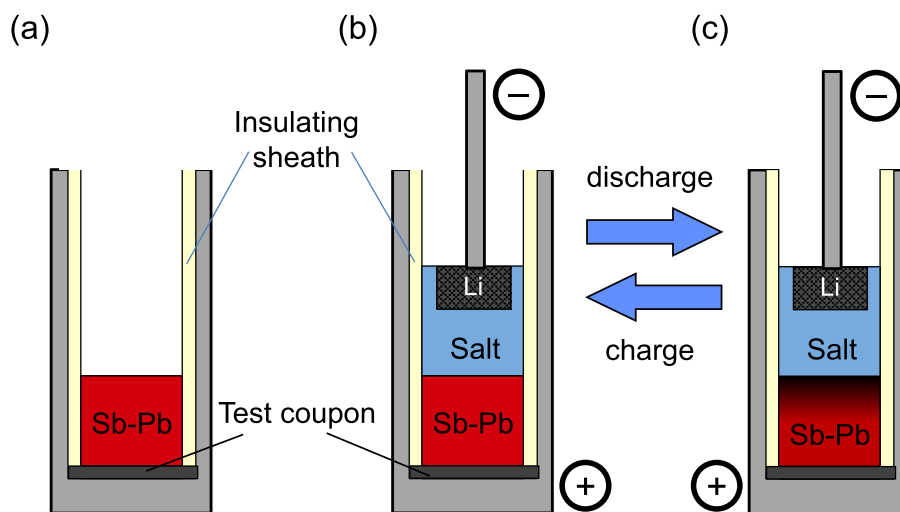


**Fig. 1.** Cross-sectional views of test conditions: (a) Sb-Pb alloy, (b) fully-charged state, and (c) operating state. The insulating sheath is boron nitride. The negative current collector consists of pure iron foam and SS18-7 rod. The positive current collector was low-carbon steel (1018).

**Table 1**  
Composition of test coupons (in wt%).

	Fe	Cr	Ni	C	Mn	Mo	Si	S	P
1018	98.36	0.06	0.04	0.09	1.03	0.01	0.01	0.35	0.06
SS301	73.54	17.41	7.29	0.09	0.91	0.22	0.5	0.01	0.026
SS430	82.16	16.6	0.29	0.04	0.44	0.06	0.39	–	0.02

steel (1018) crucible was used as the cell body. The dimensions of the low-carbon steel crucible were 25 mm in outer diameter, 83 mm in height, 77 mm in depth, and 20 mm in inner diameter. The test coupons were placed on the bottom of the cell. A boron nitride sheath, 16.3 mm inner diameter and 20 mm outer diameter, was inserted to press the test coupons down to the bottom of the crucible. The negative current collector (NCC) consisted of an 18-8 stainless steel threaded rod and a column-shaped Fe-Ni foam. The Fe-Ni foam was 13 mm in diameter, 5 mm tall, pore diameter  $\sim 380 \mu\text{m}$ . The foam NCC was positioned 15 mm above the bottom of the PCC. By surface tension the foam NCC holds lithium and keeps it away from the boron nitride. The surface area of the positive electrode was  $2.09 \text{ cm}^2$ . The cells were charge-discharge cycled at  $250 \text{ mA cm}^{-2}$  current density for 100 times using battery testers (BR2000, Arbin, and Model 4300, Maccor). All tests were done in a test vessel of the type shown in Fig. 2 at a constant temperature of  $450 \pm 0.5 \text{ }^\circ\text{C}$  under Ar atmosphere. The measured oxygen level from the outlet of the test vessel was less than 0.01 ppm. The salt was a mixture of lithium fluoride (ultra-dry 99.99%, Alfa Aesar), lithium chloride (ultra-dry 99.995%, Alfa Aesar), and lithium iodide (ultra-dry 99.999%, Alfa Aesar) prepared following the processes described in previous works [2,9,10]. The composition of the LiF-

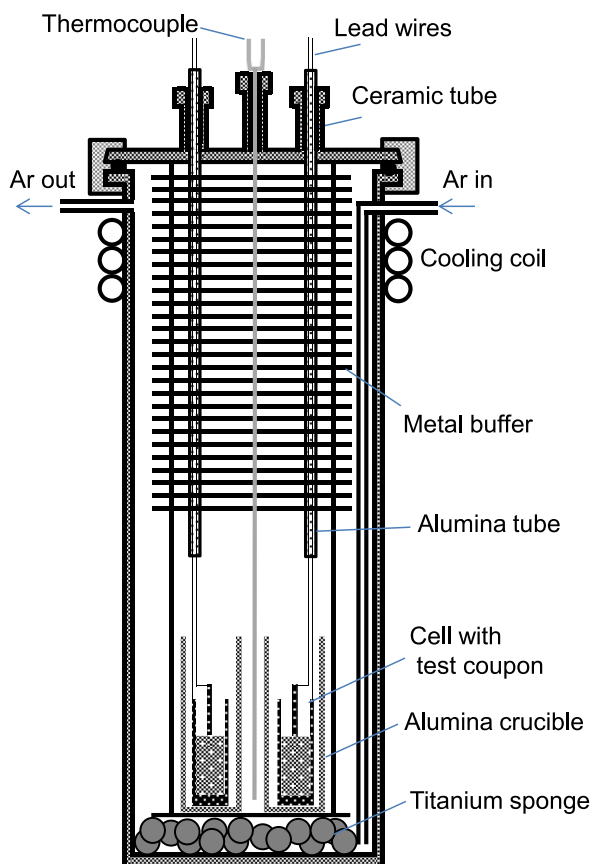


**Fig. 2.** Schematic illustration of SS304 test vessel.

LiCl-LiI molten salt electrolyte was 20–50–30 mol% ( $T_m = 430 \text{ }^\circ\text{C}$ ). The sectional specimens were analyzed by scanning electron microscopy (SEM, JEOL6610), energy dispersive X-ray spectrometry (EDS, IXRF System, Model 55i), and electron probe microanalyzer (EPMA, JEOL-JXA-8200).

### 3. Results and discussion

#### 3.1. Static corrosion of Fe, Ni, Cr in Sb-Pb alloy (fully charged cell)

We began with an evaluation of the corrosion of the steels by pure liquid Sb-Pb alloy representing a fully-charged state (Fig. 1a) Li||Sb-Pb cell. The corrosion of the PCC in liquid Sb-Pb may involve the following processes: (1) dissolution of PCC into the liquid Sb-Pb, (2) thermal and concentration gradient assisted mass transfer in PCC and liquid Sb-Pb, (3) dissolution penetration of liquid metals into solid metals with formation of intermetallic solid solutions or new compounds. To the best of our knowledge, there has been no investigation of the corrosion of stainless steels in liquid Sb-Pb alloy; accordingly, thermodynamic evaluation of metals composing steels and stainless steels, such as iron (Fe), nickel (Ni), and chromium (Cr), equilibrated with liquid Sb-Pb alloy was the first step. To evaluate the formation of intermetallic compounds, static corrosion testing of pure Fe, Ni, and Cr was carried out. The cross-sections at the interfaces between coupons and liquid metal Sb-Pb alloys after 500 h immersion are shown in Fig. 3. The layers of Fe-Sb, Ni-Sb, and Cr-Sb intermetallic alloys were observed in the cross sectional SEM shown in Fig. 3(a–c). The line scans of composition are shown in Fig. 3d–f. A small quantity of oxygen (O) and Pb were found in the intermetallic layers. These results suggest the Sb dominantly alloyed with Ni, Fe, and Cr in Sb-Pb alloys. According to the phase diagram [11–16] and composition analysis of the sample shown in Fig. 3, the intermetallic layers are considered to be  $\text{FeSb}_2$ ,  $\text{Ni}_3\text{Sb}$ ,  $\text{Ni}_5\text{Sb}_2$ ,  $\text{NiSb}_2$ ,  $\text{CrSb}$ , and  $\text{CrSb}_2$ . Layer thickness was observed to follow  $\text{Ni} > \text{Fe} > \text{Cr}$ . As the formation of intermetallic solid solutions and compounds is affected by dissolution of solid metal and penetration of liquid metal into solid metal, our data suggest that the solubilities of Fe, Ni, and Cr in Sb-Pb rank  $\text{Ni} > \text{Fe} > \text{Cr}$ , in contrast to those in a Pb and a Pb-Bi eutectic (LBE) alloy,  $\text{Ni} > \text{Cr} > \text{Fe}$  [6,7]. This difference in behavior indicates that the increase in the concentration of Sb in Sb-Pb alloy is accompanied by an increase in the solubility of Fe. These data further suggest that the nickel content of the PCC needs to be reduced.

#### 3.2. Static corrosion of low-carbon steel, SS301, and SS430

In order to elucidate the effects of the concentration of Fe, Ni, and Cr in steel and stainless steels, a low-carbon steel (1018), a FeNiCr-based stainless steel (SS301), and a FeCr-based stainless steel (SS430) were selected for the investigation. Static corrosion tests of 1018, SS301, and SS430 in the liquid Sb-Pb alloy were performed. Cross sections of coupons after 500 h immersion are shown in Fig. 4. On 1018, SS301 and SS430, layers of Fe-Sb alloy ( $\sim 100 \mu\text{m}$  in thick), Fe-Ni-Cr-Sb alloy ( $\sim 10 \mu\text{m}$  thick), and Fe-Cr-Sb ( $\sim 10 \mu\text{m}$  thick) were formed, respectively. The composition of the Fe-Sb alloy on the steel 1018 was  $\text{FeSb}_2$ . Small quantities of Cr and Ni were found in the alloys on SS301 and SS430; in contrast, almost no detectable Cr and Ni were confirmed in the Sb-Pb alloy. No clear recession was observed on SS301 and SS430.

#### 3.3. Cell performance

The corrosion of the steels and stainless steels in operating Li||Sb-Pb cells was evaluated by placing the test coupons as PCCs in cells that were charged/discharged for 500 h. The important factors

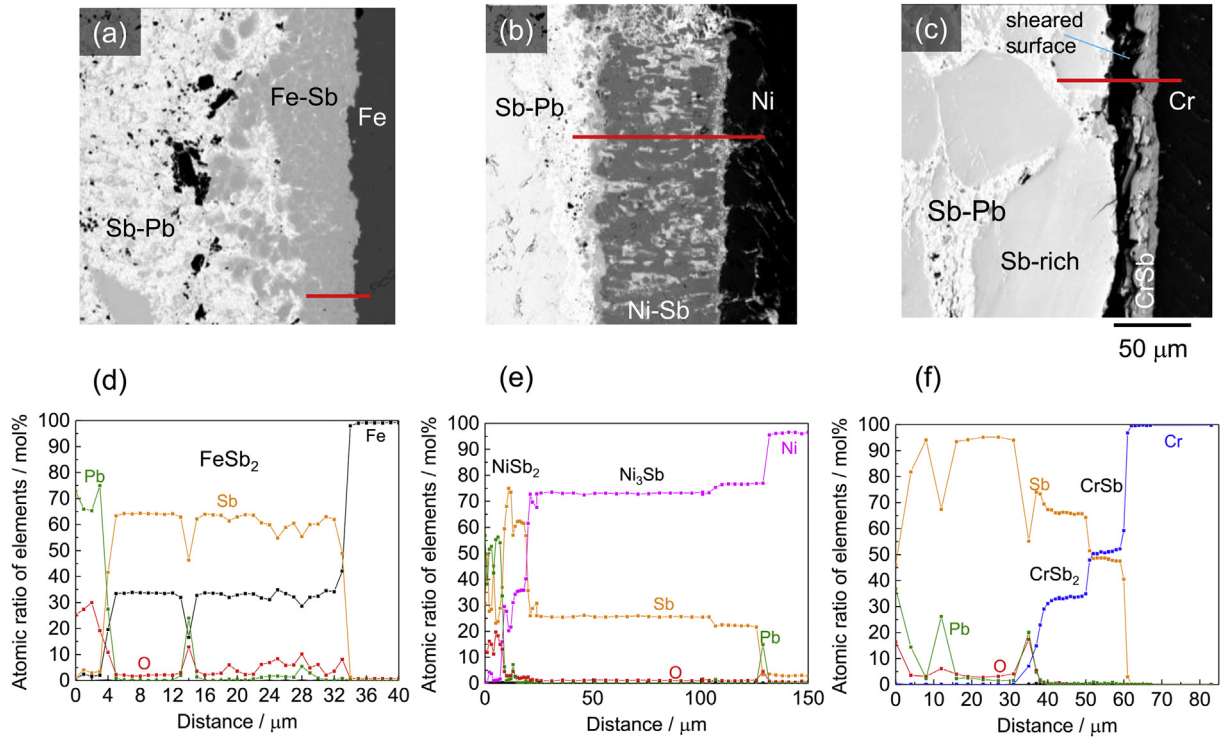


**Fig. 3.** Cross-sectional SEM images and their composition analyses (EPMA): (a) Fe, (b) Ni, (c) Cr. (d) composition analysis of Fe, (e) composition analysis of Ni, and (f) composition analysis of Cr. The operating temperature and time were 450 °C and 500 h, respectively. The composition analyses were done on the red lines in (a–c). (For interpretation of the references to colour in this figure legend, the reader is referred to the web version of this article.)

in the selection of a PCC are: (1) voltage change, (2) capacity fade, and (3) recession of PCC with cycling.

Fig. 5 (a) shows charge-discharge voltage–time traces of the cells during the 20th cycle. There was no difference in cell charge-

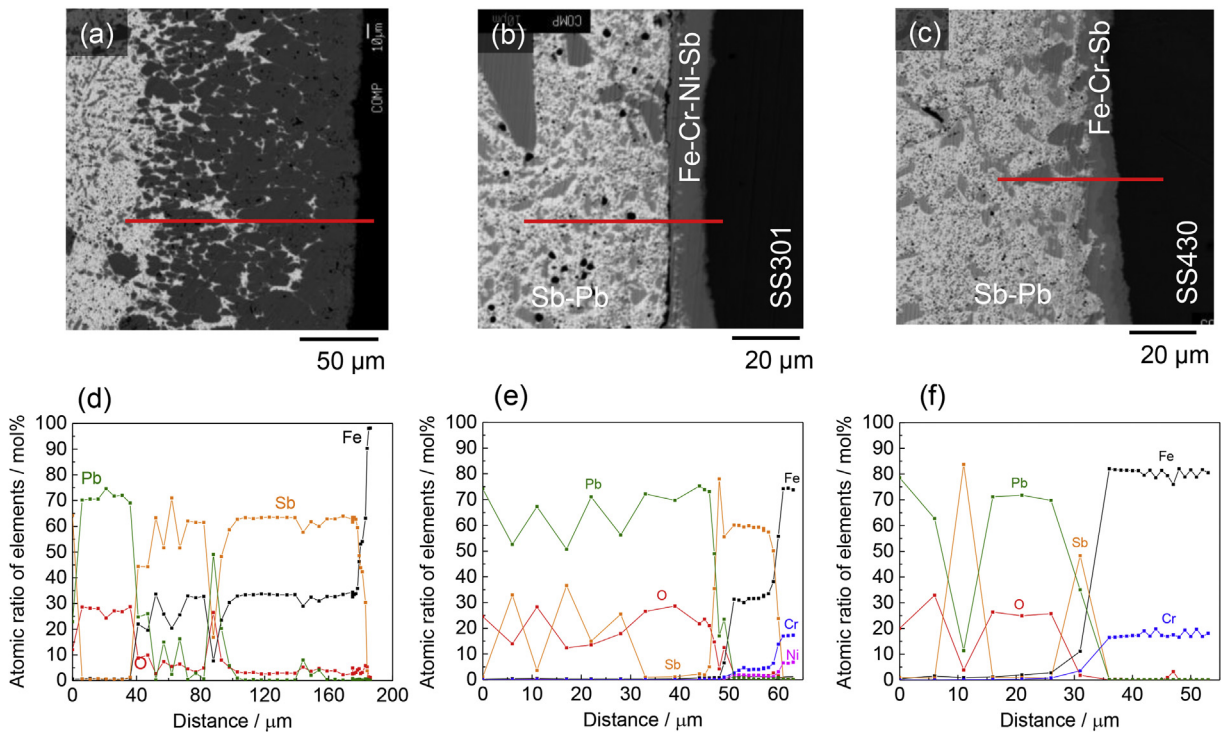


**Fig. 4.** Cross-sectional SEM images and their composition analyses (EPMA): (a) low-carbon steel, (b) SS301, (c) SS430, (d) composition analysis of low-carbon steel, (e) composition analysis of SS301, and (f) composition analysis of SS430. The operating temperature and time were 450 °C and 500 h, respectively. The composition analyses were done on the red lines in (a–c). (For interpretation of the references to colour in this figure legend, the reader is referred to the web version of this article.)

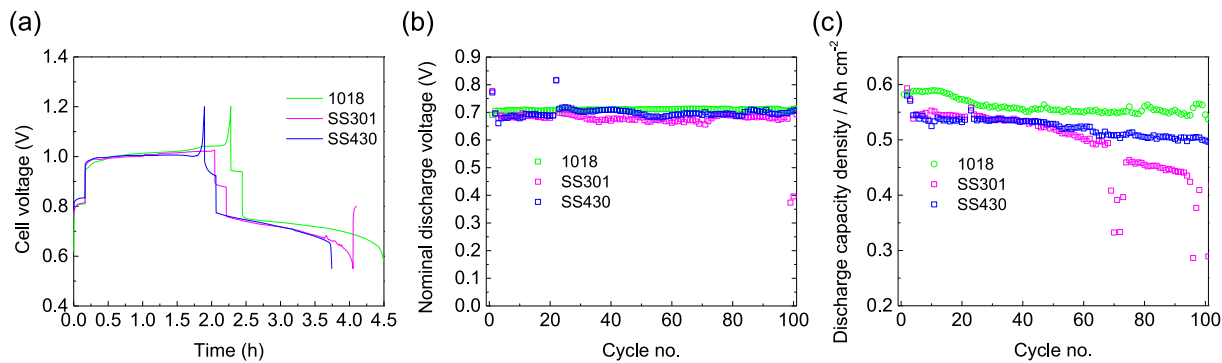


**Fig. 5.** Cell cycling performance of Li||Sb-Pb cells: (a) charge-discharge voltage-time trace of 20th cycle, (b) variation in average discharge voltage with cycling, (c) variation in discharge capacity density with cycling. Current density was  $250 \text{ mA cm}^{-2}$ .

discharge performance by changing the PCC materials in Fig. 5 (a). The nominal discharge voltage did not change with cycling with all types current collectors as shown in Fig. 5 (b). This indicates the dissolved Fe, Ni, Cr have a minor effect on the voltage of the cell. However, the discharge capacity fade rate with cycling varies with the composition of the PCC. The capacity fade rate of 1018, SS301, and SS430 were 0.05% per cycle, 0.35% per cycle, and 0.06% per cycle, respectively (Fig. 5 c). According to data available in the literature the first lithiation potentials of  $\text{FeSb}_2$  [17–19],  $\text{CrSb}_2$  [19],  $\text{NiSb}_2$  [20] at room temperature are lower than that of Sb-Pb ( $\sim 0.88 \text{ V}$ ) [2]. Furthermore, the first lithiation potentials of  $\text{FeSb}_2$  ( $\sim 0.62 \text{ V}$ ) and  $\text{CrSb}_2$  ( $\sim 0.57 \text{ V}$ ) are higher than the discharge cutoff voltage in this work ( $0.5 \text{ V}$ ). On the other hand the lithiation potential of  $\text{NiSb}_2$  is small ( $\sim 0.48 \text{ V}$ ), almost the same as the discharge

cutoff voltage. This suggests that as the cell cycles it gradually loses active Sb by forming Ni-Sb intermetallics.

### 3.4. Corrosion in cell cycling condition

After 100 cycles, the cells were cooled and sectioned. Fig. 6 shows SEM images. Obvious recession with no Fe-Sb layer was confirmed on 1018. Although the Fe-Cr-Ni-Sb layer formed on SS301, some recession occurred. In contrast, a thin uniform Fe-Cr-Sb layer was observed on SS430 which exhibited no recession. During discharge, Li alloys preferentially with Sb in the positive electrode to form Li-Sb-Pb alloys of low Pb concentration; then on charging the Li dealloys from the Li-Sb-Pb alloys [2]. This variation in lithium concentration has the potential to destroy the surface

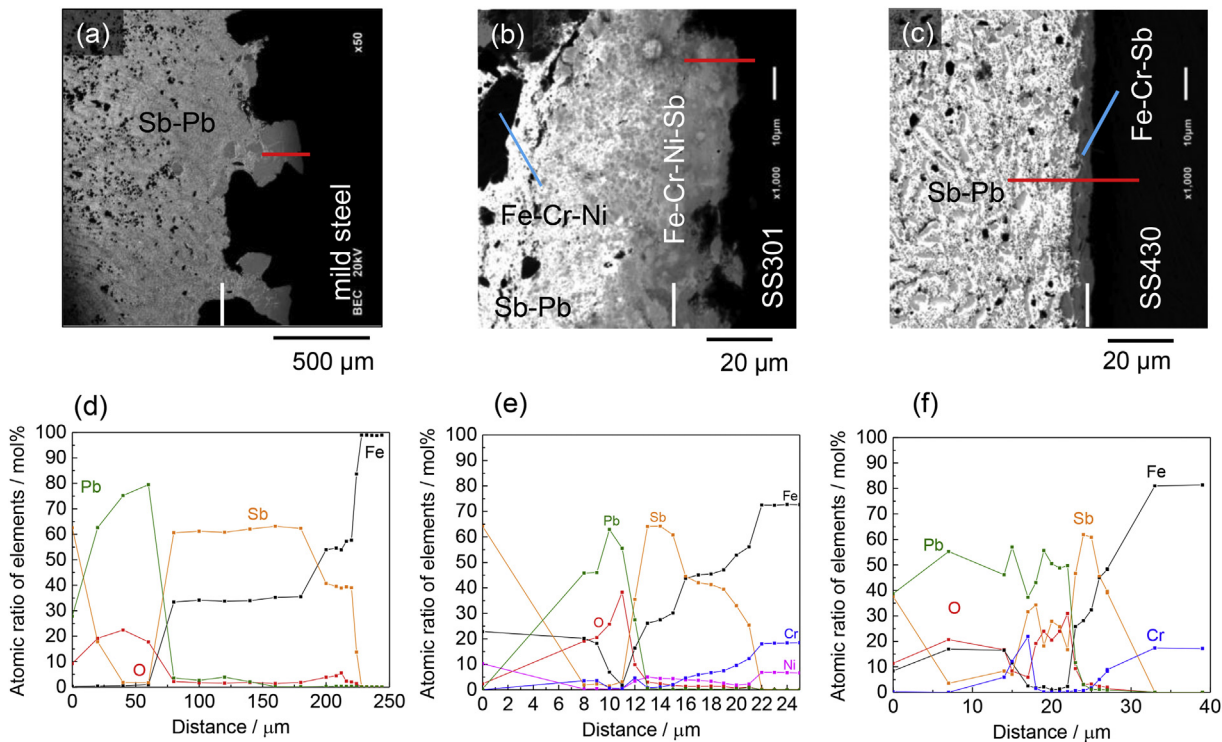


**Fig. 6.** Cross-sectional SEM images and their composition analyses (EPMA): (a) low-carbon steel, (b) SS301, (c) SS430, (d) composition analysis of low-carbon steel, (e) composition analysis of SS301, and (f) composition analysis of SS430. The operating temperature and time were  $450 \text{ }^\circ\text{C}$  and  $500 \text{ h}$ , respectively. The composition analyses were done on the red lines in (a–c). The original surfaces of the test coupons were depicted with white lines in the images. (For interpretation of the references to colour in this figure legend, the reader is referred to the web version of this article.)

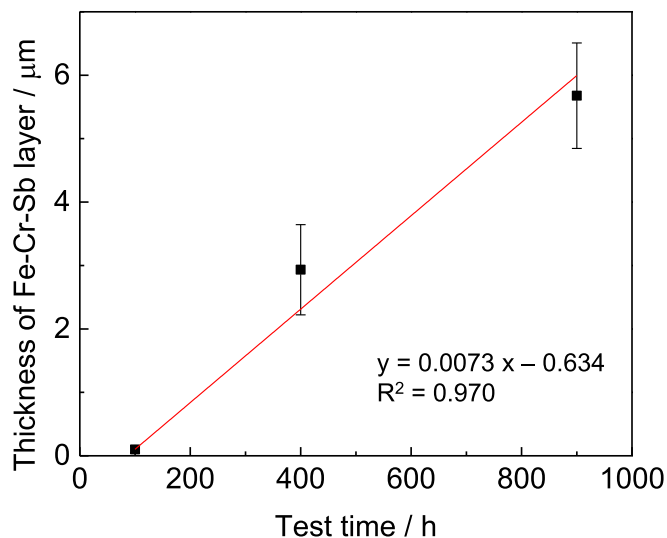


Fig. 7. Growth of Fe-Cr-Sb intermetallic layer with cycling time.

layer of Fe-Sb and Fe-Cr-Ni-Sb. However, it was determined in this study that Fe-Cr-Sb alloy is a stable intermetallic compound over the entire range of lithiation.

Furthermore, the growth rate of the Fe-Cr-Sb layer is slow as shown in Fig. 7. Even with the linear approximation, the growth rate was 63  $\mu\text{m}$  per year. These results suggest that among the materials evaluated in this work SS430 is the candidate PCC for Li||Sb-Pb LMB although the 475 °C embrittlement phenomenon is a concern.

#### 4. Conclusion

In this work, we demonstrated a concept for prolonging the service lifetime of positive current collectors in LMBs. The formation of new layers of protective Fe-Cr-Sb alloys extends the use of low-cost structural metals as cell components in LMBs without any additional processes (e.g., surface treatment). Although there was no obvious effect of embrittlement of SS430 at ~475 °C due to precipitation of Cr-enriched  $\alpha'$  phase, this will motivate us for further investigation to find a composition of stainless steel that balances ductility and corrosion resistance.

#### Acknowledgment

Financial support from the US Department of Energy, Advanced Research Projects Agency-Energy (Award No. DE-AR0000047) and Total, S.A. is gratefully acknowledged.

#### References

- [1] H. Kim, D.A. Boysen, J.M. Newhouse, B.L. Spatocco, B. Chung, P.J. Burke, D.J. Bradwell, K. Jiang, A.A. Tomaszowska, K. Wang, W. Wei, L.A. Ortiz, S.A. Barriga, S.M. Poizeau, D.R. Sadoway, *Chem. Rev.* 113 (2013) 2075–2099.
- [2] K. Wang, K. Jiang, B. Chung, T. Ouchi, P.J. Burke, D.A. Boysen, D.J. Bradwell, H. Kim, U. Muecke, D.R. Sadoway, *Nature* 514 (2014) 348–350.
- [3] P.F. Tortorelli, J.H. DeVan, J.R. Keiser, *J. Nucl. Mater.* 103 (1981) 675–680.
- [4] G.C. Burrow, M.G. Down, C. Bagnall, *J. Nucl. Mater.* 103 (1981) 657–662.
- [5] Q. Jiapu, C. Jiming, C. Jinbiao, X. Zengyu, W. Weihao, P. Chuanjie, *J. Nucl. Mater.* 179 (1991) 603–606.
- [6] J. Zhang, N. Li, *J. Nucl. Mater.* 373 (2008) 351–377.
- [7] N. Li, *J. Nucl. Mater.* 300 (2002) 73–81.
- [8] M. Machut, K. Sridharan, N. Li, S. Ukai, T. Allen, *J. Nucl. Mater.* 371 (2007) 134–144.
- [9] T. Ouchi, H. Kim, B.L. Spatocco, D.R. Sadoway, *Nat. Commun.* 7 (2016) 10999.
- [10] T. Ouchi, H. Kim, X. Ning, D.R. Sadoway, *J. Electrochem. Soc.* 161 (2014) A1898–A1904.
- [11] H. Okamoto, Fe-Sb (Iron-Antimony) phase diagram, in: P. Villars, H. Okamoto, K. Cenzual (Eds.), *ASM Alloy Phase Diagrams Database*, ASM International, Materials Park, OH, 2016. <http://www.asminternational.org>.
- [12] G.H. Cha, S.Y. Lee, P. Nash, Ni-Sb (Nickel-Antimony) phase diagram, in: P. Villars, H. Okamoto, K. Cenzual (Eds.), *ASM Alloy Phase Diagrams Database*, ASM International, Materials Park, OH, 2016. <http://www.asminternational.org>.
- [13] M. Venkatraman, J.P. Neumann, Cr-Sb (Chromium-Antimony) phase diagram, in: P. Villars, H. Okamoto, K. Cenzual (Eds.), *ASM Alloy Phase Diagrams Database*, ASM International, Materials Park, OH, 2016. <http://www.asminternational.org>.
- [14] E. Isaac, G. Tammann, Fe-Pb (Iron-lead) phase diagram, in: P. Villars, H. Okamoto, K. Cenzual (Eds.), *ASM Alloy Phase Diagrams Database*, ASM International, Materials Park, OH, 2016. <http://www.asminternational.org>.
- [15] P. Nash, Ni-Pb (Nickel-Lead) phase diagram, in: P. Villars, H. Okamoto, K. Cenzual (Eds.), *ASM Alloy Phase Diagrams Database*, ASM International, Materials Park, OH, 2016. <http://www.asminternational.org>.
- [16] M. Venkatraman, J.P. Neumann, Cr-Pb (Chromium-Lead) phase diagram, in: P. Villars, H. Okamoto, K. Cenzual (Eds.), *ASM Alloy Phase Diagrams Database*, ASM International, Materials Park, OH, 2016. <http://www.asminternational.org>.
- [17] C. Villevieille, C.M. Ionica-Bousquet, B. Fraisse, D. Zitoun, M. Womes, J.C. Jumas, L. Monconduit, *Solid State Ion.* 192 (2011) 351–355.
- [18] C. Villevieille, B. Fraisse, M. Womes, J.-C. Jumas, L. Monconduit, *J. Power Sources* 189 (2009) 324–330.
- [19] Cheol-Min Park, Hun-Joon Sohn, *Electrochim. Acta* 55 (2010) 4987–4994.
- [20] C. Villevieille, C.-M. Ionica-Bousquet, B. Ducourant, J.-C. Jumas, L. Monconduit, *J. Power Sources* 172 (2007) 388–394.